Modeling of Tunable Electronic Waveguide Devices in Graphene using Conservative Higher-Order Time Stepping

Emile Vanderstraeten, Dries Vande Ginste, *Senior Member, IEEE,*

***Abstract*—An accurate technique leveraging conservative higher-order time stepping is proposed to analyze electrostatically induced waveguides in graphene. These highly tunable one-dimensional (1D) electronic channels are a promising interconnect alternative for graphene nanoribbons (GNRs) and carbon nanotubes (CNTs) to be used in future integrated circuits (ICs). A detailed discussion of the eigenmodes of these waveguides is presented and specific attention is paid to the orthogonality relations, which are remarkably similar to their electromagnetic counterpart. Furthermore, it is demonstrated that the addition of a vector potential does not affect the long-term properties of the time stepping scheme. To showcase the accuracy and applicability of the constructed technique two practical electronic waveguide devices are simulated: a dot resonator and a 50/50 splitter containing no bends. The dot resonator exhibits frequency selective behavior that proves to be tunable by both the scalar and vector potential, while the desired output characteristic is obtained for the splitter after carefully tuning the confining potentials.**

***Index Terms*—Graphene, higher-order time stepping, waveguides, quantum mechanical modeling**

I. Introduction

One of the main challenges in future IC-design is to make the Cu interconnects comply with the ever decreasing transistor size. At the nanoscale the resistance of the Cu interconnects increases faster than linear with shrinking dimensions because of the increased impact of surface scattering and grain-boundary scattering [1], [2], which, as a consequence, negatively affects the time delay and the power dissipation. Moreover, the increased Joule heating induces a rise in temperature. As the electromigration lifetime deteriorates exponentially with temperature, the maximum current-carrying capacity of these scaled interconnects is severely limited [3], [4].

Alternatives for Cu in future interconnects are carbon nanotubes (CNTs) and graphene nanoribbons (GNRs). Besides having a large mean free path, which is of the orders of micrometers, these carbon allotropes exhibit a current-carrying capacity that is more than two orders of magnitude larger than that of Cu, thereby mitigating the reliability concerns related to electromigration that plague the Cu nanointerconnects [4], [5]. However, precise control of the diameter and chirality is still challenging for CNTs, while GNRs suffer from edge scattering [6].

Another approach of creating quasi-1D electronic channels in graphene is by means of a confining electrostatic potential (see Fig. 1). Compared to GNRs, edge scattering is avoided by positioning the electrostatic potential V away from the boundaries. Furthermore, these 1D channels are highly tunable as their properties can be modified by simply changing this electrostatic potential V of the gate contact [7], [8]. Confining electrons in 1D potentials in graphene can be understood in the same way as trapping light in optical fibers. Because of their linear dispersion relation and long mean free path, charge carriers in graphene behave in close analogy with light. They are refracted at the interface between regions with different electrostatic potential in the same way as light undergoes refraction when crossing the boundary between media with different refractive index [9], [10]. Several devices have been proposed that simultaneously exploit this analogy and the peculiar properties of graphene such as lenses [11], Fabry-Pérot resonators [12], transistors [13], [14], and gratings [15], [16], while the analogs of Mie scattering, whispering gallery modes and the Goos-Hänchen effect have been described as well in [17]–[20]. The quality of the graphene layer is of fundamental importance for the experimental realization of these devices. An important breakthrough in this regard is the usage of hBN over SiO_2 as substrate for the graphene layer. When SiO_2 is employed, the graphene layer suffers considerably from surface roughness because the SiO_2-layer is amorphous [21]. hBN on the other hand is an atomically flat crystalline structure of which the lattice mismatch with graphene is only 1.8%, resulting in a smoother graphene layer [22]. In addition, charge inhomogeneities located in the substrate induce regions with a net positive or negative charge. These electron/hole puddles manifest themselves as local shifts of the Dirac points which are of the order of 5 meV for hBN compared to 50 meV for SiO_2 [22], [23].

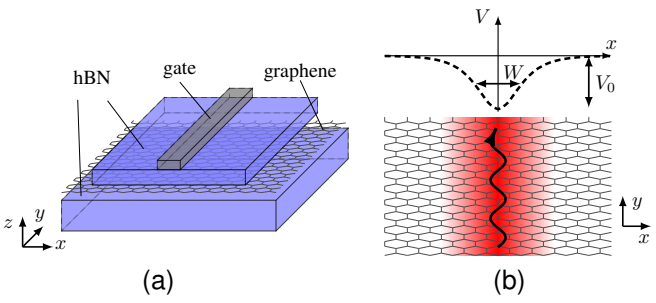

Fig. 1. (a) Illustration of an electronic waveguide consisting of a graphene layer encapsulated between two hBN layers (a substrate layer and an insulating layer). The gate electrode is used to define the confining potential V. (b) Visualization of the confined propagation of an electron in a potential well, with width W and depth V_0, in graphene.

Consequently, for the eigenmodes in the waveguides to be well defined, the confining potential should be much larger than these random fluctuations. Furthermore, the number of modes scales approximately with the depth V_0 and width W of the potential and thus, the confining potential of a single mode waveguide should be sufficiently narrow [7]. When CNTs are employed as gate, these conditions can be met [24], paving the way for highly tunable interconnects and electronic waveguide devices in graphene.

In an earlier conference contribution [25], we have presented a quantum mechanical, first-principles technique, based on higher-order conservative partitioned Runge-Kutta (PRK) time stepping for the (2+1)D Dirac equation, to analyze the aforementioned interconnects structures. In this paper, this time stepping algorithm is extended to include vector potentials as well. These vector potentials are an additional degree of freedom, besides the shape of the electrostatic potential, that can be used to tune the properties of the interconnects. We propose a scheme that discretizes the additional terms in the (2+1)D Dirac equation, which has become more intricate, in such a way that the superior long-term properties of the numerical scheme are still retained. In addition, in this paper, the eigenvalue problem is carefully investigated and the orthogonality relations of the eigenmodes are discussed as they are required for the calculations of the transmission function. The novel numerical technique is applied to two practical examples: a dot resonator and a splitter, where the focus is on the intricacies related to the Dirac system. For the dot resonator the results are compared to those obtained via another second order time stepping scheme [26], thereby validating and illustrating the accuracy of the advocated technique.

The paper is organized as follows. In Section II, the theoretical aspect of the electronic waveguides' eigenvalue problem is investigated. An innerproduct is introduced, allowing us to derive an orthogonality relation between the eigenmodes. The numerical technique itself is explained in Section III. The time stepping algorithm of [27] is adapted to include vector potentials without sacrificing its main advantages and it is clarified how the transmission as a function of the energy is determined from time-domain simulations. Two relevant examples, a dot resonator and splitter, are treated in Section IV. Finally, the paper is concluded in Section V.

II. Electrostatically induced waveguides in graphene

To model these electrostatically induced waveguides, we assume that the electrodes are separated from the graphene layer by means of a sufficiently thick insulating hBN layer such that tunneling can be neglected. Additionally, the scalar potential V and vector potential $\boldsymbol{a}$ should be slowly varying on the lattice scale to avoid intervalley scattering [9]. If these two requirements are met, then, at low energies, the motion of an electron in graphene is accurately described by the following (2+1)D Dirac equation

$$i\hbar\frac{\partial}{\partial t}\boldsymbol{\Psi} = \left[v_F\boldsymbol{\sigma}\cdot\left(\boldsymbol{p} - q\,\boldsymbol{a}(x,y)\right) + V(x,y)\right]\boldsymbol{\Psi}, \qquad (1)$$

where $\boldsymbol{\Psi} = \left(\begin{smallmatrix} u \\ v \end{smallmatrix}\right)$ is the two-component wave function, which is often called the Dirac spinor. The 2D vector $\boldsymbol{\sigma}$ contains two elements, the Pauli spin matrices $\sigma_x = \left(\begin{smallmatrix} 0 & 1 \\ 1 & 0 \end{smallmatrix}\right)$ and $\sigma_y = \left(\begin{smallmatrix} 0 & -i \\ i & 0 \end{smallmatrix}\right)$. The momentum operator is represented by $\boldsymbol{p} = -i\hbar\boldsymbol{\nabla}$. The constant v_F is the Fermi velocity and in the rest of this paper the value of 10^6 m/s is utilized. Note that if we substitute a plane wave of the form $\boldsymbol{\Psi} = \boldsymbol{A}\,e^{i(\boldsymbol{k}\cdot\boldsymbol{r} - E\,t/\hbar)}$ into (1) with both the scalar and vector potential equal to zero, the linear dispersion relation $E = \pm\hbar v_F|\boldsymbol{k}|$ is obtained, which lies at the basis of the analogy with electromagnetic phenomena. Similar as other quantum mechanical equations, such as the Schrödinger equation for example, the wave function $\boldsymbol{\Psi}$ itself is not measurable. Hence, observables, such as the probability density and probability current density need to be introduced, which are, in the case of the (2+1)D Dirac equation, given by

$$P = \boldsymbol{\Psi}^\dagger\boldsymbol{\Psi} \qquad (2)$$

and

$$\boldsymbol{j} = \boldsymbol{\Psi}^\dagger v_F\,\boldsymbol{\sigma}\boldsymbol{\Psi}, \qquad (3)$$

respectively, where $\boldsymbol{\Psi}^\dagger$ denotes the hermitian conjugate of $\boldsymbol{\Psi}$.

Charged particles in 2D graphene can be confined in a 1D channel by means of an electrostatic potential. Therefore, assume that V is y-independent and that $\boldsymbol{a}$ is zero. Consequently, substitute $\boldsymbol{\Psi} = \begin{pmatrix} \tilde{u}(x) \\ \tilde{v}(x) \end{pmatrix} e^{i(k_y\,y - E\,t/\hbar)}$ into (1), yielding

$$\begin{pmatrix} \frac{\partial}{\partial x} & \frac{E-V(x)}{\hbar\,v_F} \\ \frac{E-V(x)}{\hbar\,v_F} & -\frac{\partial}{\partial x} \end{pmatrix}\begin{pmatrix} \tilde{u}(x) \\ -i\,\tilde{v}(x) \end{pmatrix} = k_y\begin{pmatrix} \tilde{u}(x) \\ -i\,\tilde{v}(x) \end{pmatrix}. \qquad (4)$$

Equation (4) constitutes an eigenvalue problem where the energy E is a parameter and $V(x)$ the confining potential. When an eigenvalue k_y is found for which (4) holds, then the corresponding $\begin{pmatrix} \tilde{u}(x) \\ -i\,\tilde{v}(x) \end{pmatrix}$ is called the eigenmode. For a real eigenvalue, the amplitude of the related eigenmode propagates unabated along the y-axis; only its phase changes. Note that owing to the specific form of (4), real k_y implies that both $\tilde{u}$ and $-i\,\tilde{v}$ are real as well. For several discontinuous [28]–[30] and smooth [7], [31], [32] electrostatic potentials $V(x)$ it has been demonstrated analytically that real eigenvalues and eigenmodes exist that comply with (4). Remark that when k_y and $\begin{pmatrix} \tilde{u}(x) \\ -i\,\tilde{v}(x) \end{pmatrix}$ satisfy (4), then $-k_y$ and $\begin{pmatrix} i\,\tilde{v}(x) \\ \tilde{u}(x) \end{pmatrix}$ also obey (4) and thus, are also an eigenvalue and eigenmode.

In a next step, we investigate the orthogonality relations between the eigenmodes $\tilde{\boldsymbol{\Psi}}_1$ and $\tilde{\boldsymbol{\Psi}}_2$, with their respective eigenvalues $k_{y,1}$ and $k_{y,2}$, as it will be relevant for the construction of the numerical technique in Section III. Therefore, consider the innerproduct

$$\langle\tilde{\boldsymbol{\Psi}}_1, \tilde{\boldsymbol{\Psi}}_2\rangle = \int_{-\infty}^{+\infty}\tilde{\boldsymbol{\Psi}}_2^\dagger\,v_F\,\sigma_y\tilde{\boldsymbol{\Psi}}_1\mathrm{d}x. \qquad (5)$$

Comparison with the probability current density $\boldsymbol{j}$ of (3) indicates that the innerproduct of a mode with itself equals the probability current flowing through a cross section of the waveguide. Consequently, the eigenmodes can be normalized by requiring that this probability current equals one. By substituting (4) into (5) and invoking integration by parts, the relation

$$\langle\tilde{\boldsymbol{\Psi}}_1, \tilde{\boldsymbol{\Psi}}_2\rangle = \frac{k_{y,2}^*}{k_{y,1}}\langle\tilde{\boldsymbol{\Psi}}_1, \tilde{\boldsymbol{\Psi}}_2\rangle \qquad (6)$$

is obtained, with $k_{y,2}^*$ being the complex conjugate of $k_{y,2}$. As a consequence, eigenmodes that are related to real eigenvalues are orthogonal with respect to all other eigenmodes, i.e., $\langle \tilde{\boldsymbol{\Psi}}_1, \tilde{\boldsymbol{\Psi}}_2 \rangle = 0$, as long as the innerproduct (5) is employed.[1] Furthermore, the total probability current flowing through the waveguide is the sum of the probability current associated with each individual mode.

The above discussion of the innerproduct resembles that of electromagnetic waveguides. In that case, for the modes $(\boldsymbol{E}_1, \boldsymbol{H}_1)$ and $(\boldsymbol{E}_2, \boldsymbol{H}_2)$, the innerproduct

$$\int_S (\boldsymbol{E}_1 \times \boldsymbol{H}_2^*) \cdot \boldsymbol{u}_n \, \mathrm{d}S \tag{7}$$

is employed to define *power* orthogonality in the presence of *lossless* media [33].[2] Given its relation with the Poynting vector, the innerproduct of an eigenmode with itself represents the total power flow propagating through the cross section of the waveguide, which is analogous to the total probability current for the graphene waveguides. Similarly, the total power flow is equal to the sum of the individual powers carried by the eigenmodes.

III. Numerical method

In this section, we extend the higher-order conservative time stepping of [25], [27] to include vector potentials as well and, based on the theoretical analogy with electromagnetism, further elaborate how it can be employed to examine the transmission through electrostatically induced waveguides in graphene.

To discretize the wave function $\boldsymbol{\Psi}$, we start from the staggered spatial grid employed in [26]. The simulation domain of size $L_x \times L_y$ is divided into $N_x \times N_y$ unit cells of size $\Delta x \times \Delta y$. Within each unit cell (i, j), the component u of $\boldsymbol{\Psi}$ is located at two positions: $(i\Delta x, j\Delta y)$ and $((i+1/2)\,\Delta x, (j+1/2)\,\Delta y)$. The values of u at these respective positions are stored in the vectors $\boldsymbol{u}_1$ and $\boldsymbol{u}_2$. Similarly, the component v of Ψ is defined at locations $((i+1/2)\,\Delta x, j\Delta y)$ and $(i\Delta x, (j+1/2)\,\Delta y)$, and contained in the vectors $\boldsymbol{v}_1$ and $\boldsymbol{v}_2$, respectively. We propose a novel stencil on this grid, including both scalar and vector potential. To reduce dispersion errors, the spatial derivatives of (1) are approximated by fourth-order central differences, yielding

$$i\hbar \frac{\mathrm{d}}{\mathrm{d}t} \begin{pmatrix} \boldsymbol{u}_1 \\ \boldsymbol{u}_2 \\ \boldsymbol{v}_1 \\ \boldsymbol{v}_2 \end{pmatrix} = (\boldsymbol{H}_1 + \boldsymbol{H}_2) \begin{pmatrix} \boldsymbol{u}_1 \\ \boldsymbol{u}_2 \\ \boldsymbol{v}_1 \\ \boldsymbol{v}_2 \end{pmatrix}, \tag{8}$$

with

$$\boldsymbol{H}_1 = \hbar\, v_F \begin{pmatrix} \frac{\boldsymbol{V}_{u_1}}{\hbar\, v_F} & 0 & -i\boldsymbol{D}_x & -\boldsymbol{D}_y \\ 0 & \frac{\boldsymbol{V}_{u_2}}{\hbar\, v_F} & \boldsymbol{D}_y^T & i\boldsymbol{D}_x^T \\ i\boldsymbol{D}_x^T & \boldsymbol{D}_y & \frac{\boldsymbol{V}_{v_1}}{\hbar\, v_F} & 0 \\ -\boldsymbol{D}_y^T & -i\boldsymbol{D}_x & 0 & \frac{\boldsymbol{V}_{v_2}}{\hbar\, v_F} \end{pmatrix}, \tag{9}$$

$$\boldsymbol{H}_2 = \frac{q v_F}{2} \begin{pmatrix} 0 & \boldsymbol{L} \\ \boldsymbol{L}^\dagger & 0 \end{pmatrix} \tag{10}$$

and

$$\boldsymbol{L} = \begin{pmatrix} i\boldsymbol{a}_{y,u_1}\boldsymbol{A}_x + i\boldsymbol{A}_x\boldsymbol{a}_{y,v_1} & -\boldsymbol{a}_{x,u_1}\boldsymbol{A}_y - \boldsymbol{A}_y\boldsymbol{a}_{x,v_2} \\ -\boldsymbol{a}_{x,u_2}\boldsymbol{A}_y^T - \boldsymbol{A}_y^T\boldsymbol{a}_{x,v_1} & i\boldsymbol{a}_{y,u_2}\boldsymbol{A}_x^T + i\boldsymbol{A}_x^T\boldsymbol{a}_{y,v_2} \end{pmatrix}. \tag{11}$$

The matrices $\boldsymbol{V}_{u_1}, \boldsymbol{V}_{u_2}, \boldsymbol{V}_{v_1}$, and $\boldsymbol{V}_{v_2}$ are diagonal matrices containing the values of the electrostatic potential at the locations associated with $\boldsymbol{u}_1, \boldsymbol{u}_2, \boldsymbol{v}_1$, and $\boldsymbol{v}_2$, respectively. The matrices $\boldsymbol{a}_x$ and $\boldsymbol{a}_y$ are constructed in the same way. The matrix $\boldsymbol{D}_x = \tilde{\boldsymbol{D}}_x \otimes \boldsymbol{I}$, with $\otimes$ the tensorproduct and

$$\left[\tilde{\boldsymbol{D}}_x\right]_{i,j} = \frac{1}{24\Delta x} \left(\delta_{i,j-2} - 27\,\delta_{i,j-1} + 27\,\delta_{i,j} - \delta_{i,j+1}\right), \tag{12}$$

with $\delta_{i,j}$ the Kronecker delta, represents the discrete analog of the spatial derivative along x, and likewise for $\boldsymbol{D}_y = \boldsymbol{I} \otimes \tilde{\boldsymbol{D}}_y$, while $\boldsymbol{A}_x = \tilde{\boldsymbol{A}}_x \otimes \boldsymbol{I}$ is an averaging operator with

$$\left[\tilde{\boldsymbol{A}}_x\right]_{i,j} = \frac{1}{16} \left(-\delta_{i,j-2} + 16\,\delta_{i,j-1} + 16\,\delta_{i,j} - \delta_{i,j+1}\right), \tag{13}$$

and likewise for $\boldsymbol{A}_y = \boldsymbol{I} \otimes \tilde{\boldsymbol{A}}_y$. Remark that the employed discretization procedure retains the hermiticity of the Hamiltonian $\boldsymbol{H}_1 + \boldsymbol{H}_2$, which is a fundamental property of the system. In addition, we now split the components of the wave function into real and imaginary part, rewriting (8) as

$$\frac{\mathrm{d}\boldsymbol{q}}{\mathrm{d}t} = \boldsymbol{K}\boldsymbol{p}\,, \quad \frac{\mathrm{d}\boldsymbol{p}}{\mathrm{d}t} = -\boldsymbol{K}^T\boldsymbol{q}, \tag{14}$$

with

$$\boldsymbol{q} = \begin{pmatrix} \mathrm{Im}(\boldsymbol{u}_1) \\ \mathrm{Re}(\boldsymbol{u}_2) \\ \mathrm{Re}(\boldsymbol{v}_1) \\ \mathrm{Im}(\boldsymbol{v}_2) \end{pmatrix}, \quad \boldsymbol{p} = \begin{pmatrix} \mathrm{Re}(\boldsymbol{u}_1) \\ \mathrm{Im}(\boldsymbol{u}_2) \\ \mathrm{Im}(\boldsymbol{v}_1) \\ \mathrm{Re}(\boldsymbol{v}_2) \end{pmatrix}. \tag{15}$$

Starting from (8)-(11) the expression for $\boldsymbol{K}$ is readily derived. Owing to the specific form of (14), an explicit symplectic PRK time integrator can be employed [34]. One timestep from $t = n\Delta t$ to $t = (n+1)\,\Delta t$ corresponds to

$$\begin{array}{cc} \boldsymbol{Q}^{n,0} = \boldsymbol{q}^n & \boldsymbol{P}^{n,1} = \boldsymbol{p}^n \\ \boldsymbol{Q}^{n,1} = \boldsymbol{Q}^{n,0} + \Delta t\, B_1\, \boldsymbol{K}\boldsymbol{P}^{n,1} & \boldsymbol{P}^{n,2} = \boldsymbol{P}^{n,1} - \Delta t\, b_1\, \boldsymbol{K}^T\boldsymbol{Q}^{n,1} \\ \boldsymbol{Q}^{n,2} = \boldsymbol{Q}^{n,1} + \Delta t\, B_2\, \boldsymbol{K}\boldsymbol{P}^{n,2} & \boldsymbol{P}^{n,3} = \boldsymbol{P}^{n,2} - \Delta t\, b_2\, \boldsymbol{K}^T\boldsymbol{Q}^{n,2} \\ \vdots & \vdots \\ \boldsymbol{Q}^{n,s} = \boldsymbol{Q}^{n,s-1} + \Delta t\, B_s\, \boldsymbol{K}\boldsymbol{P}^{n,s} & \boldsymbol{P}^{n,s+1} = \boldsymbol{P}^{n,s} - \Delta t\, b_s\, \boldsymbol{K}^T\boldsymbol{Q}^{n,s} \\ \boldsymbol{q}^{n+1} = \boldsymbol{Q}^{n,s} & \boldsymbol{p}^{n+1} = \boldsymbol{P}^{n,s+1} \end{array}, \tag{16}$$

where the intermediate values are denoted by capital letters. The constants B_m and b_m, with m ranging from 1 to s, the total number of substeps, fully characterize the PRK method. The one used in the rest of this paper agrees with the fourth-order method employed in [27], [35]. Remark that

[1] Remark that in (5), instead of the hermitian conjugate $\tilde{\boldsymbol{\Psi}}_2^\dagger$, the transpose $\tilde{\boldsymbol{\Psi}}_2^T$ could be used as well. One can check that a real eigenmode still stays orthogonal with respect to all other eigenmodes. However, the physical meaning of the innerproduct of a mode with itself is lost and, hence, in the remainder we continue to use (5).

[2] In the general situation, thus in the presence of *lossy* media, all eigenmodes are orthogonal with respect to each other if as innerproduct the unconjugated form of (7), with $\boldsymbol{H}_2^*$ replaced by $\boldsymbol{H}_2$, is used [33].

the spatial discretization proposed in (8)-(13) introduces the vector potential in the stencil in such a way that the structure of (14) has not changed compared to [27] (only the structure of matrix K has been modified) and thus, it remains a Poisson system. Consequently, following the same steps as [27], it is readily verified *analytically* that this time stepping technique conserves the total probability density and total energy of the system. These excellent conservation properties allow us to perform long-term simulations, which are needed for the accurate analysis of waveguide structures. In this paper, a *resonant* device (see Section IV-A) is modeled, which especially relies on the aforementioned properties of the novel scheme.

In the same way, the stability of the scheme also follows from [27], where it was derived that PRK timestepping applied to the set of equations (14) results in a stable algorithm as long as

$$\Delta t < \frac{C_{\text{PRK}}}{\sqrt{\rho\left(\boldsymbol{K}\boldsymbol{K}^T\right)}}, \tag{17}$$

with $\rho\left(\boldsymbol{K}\boldsymbol{K}^T\right)$ the spectral radius of the matrix $\boldsymbol{K}\boldsymbol{K}^T$ and C_{PRK} a constant that depends on the used values for B_m and b_m. For the employed fourth-order method it equals 3.0299. An easier-to-handle stability condition, i.e., which does not necessitate the computation of the spectral radius of $\boldsymbol{K}\boldsymbol{K}^T$, can be obtained by using suitable estimates [27].

The main property of interest is the transmission of the current from one point to another as a function of energy E of the charge carriers. To determine this function the following procedure is adopted. As source, a single eigenmode is injected into the waveguide in the positive y-direction in a region with constant cross section. This eigenmode is determined numerically by means of

$$\begin{pmatrix} \tilde{\boldsymbol{D}}_x & \frac{E-\boldsymbol{V}_{v_1}}{\hbar v_F} \\ \frac{E-\boldsymbol{V}_{u_1}}{\hbar v_F} & \tilde{\boldsymbol{D}}_x^T \end{pmatrix} \begin{pmatrix} \tilde{\boldsymbol{u}}_1 \\ \tilde{\boldsymbol{v}}_1 \end{pmatrix} = k_y \begin{pmatrix} \tilde{\boldsymbol{A}}_x & 0 \\ 0 & \tilde{\boldsymbol{A}}_x^T \end{pmatrix} \begin{pmatrix} \tilde{\boldsymbol{u}}_1 \\ \tilde{\boldsymbol{v}}_1 \end{pmatrix}, \tag{18}$$

which is the discretized equivalent of (4). To make this calculation compatible with the time stepping method, the same staggered grid and fourth-order approximations are employed. The time dependency of the eigenmode $e^{iEt/\hbar}$ is modulated by an additional gaussian

$$\frac{1}{\sqrt{2\pi}\sigma_t} e^{-\frac{(t-t_0)^2}{2\sigma_t^2}}, \tag{19}$$

with mean t_0 and standard deviation σ_t, making the duration of the source finite in time. To determine the transmission, an observer is positioned in a region with constant cross section. There, the values of $\boldsymbol{u}_1$ and $\boldsymbol{v}_1$ are transformed to the energy domain by means of a Fast Fourier transform and divided by the spectral content of the source. For each energy value, the wave function is a linear combination of different eigenmodes. To extract an expansion coefficient of this linear combination, the innerproduct (5) of the wave function with the relevant eigenmode is taken, which, subsequently, is divided by the norm of this eigenmode. Multiplying this expansion coefficient with its complex conjugate yields the transmission from source to observer (as a function of the energy). With this approach, a single simulation run in the time domain provides us with the transmission function for the desired range of energies.

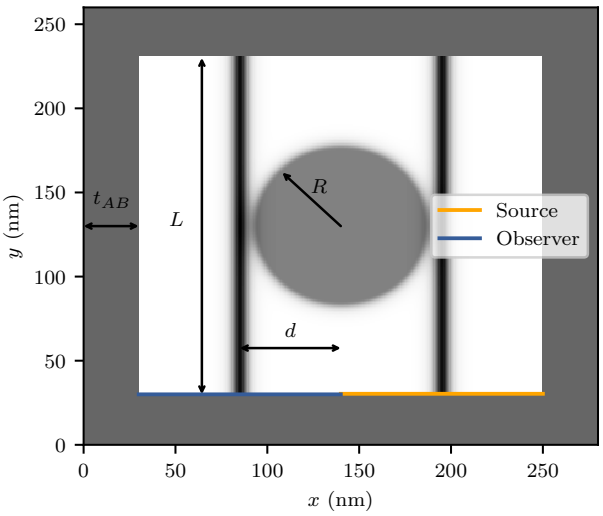

Fig. 2. Simulation setup of a dot resonator coupled to two straight interconnects in graphene.

IV. Results

A. Dot resonator

Electromagnetic ring resonators have seen widespread use as spectral filters and sensors [36]. Hence, an electrical analog in graphene constitutes a convenient building block for future (more intricate) devices. However, ring-like potentials have not been realized yet in graphene. Therefore, we shift our attention to dot resonators instead, which yield very similar results. The eigenmodes of a dot, also called whispering gallery modes, have been probed by means of a scanning tunneling microscope in [18]. In [19], a dot was positioned in a graphene constriction that was connected to a drain and source electrode and strong signatures of whispering gallery modes were observed in the current through the constriction. However, a less invasive and more tunable approach to exploit these resonances is to couple the dot to an electrostatically induced waveguide as the coupling between the dot and the waveguide can be tweaked by simply changing the electrostatic potentials [19].

The simulation setup of the dot resonator structure that is studied here is given in Fig. 2. To account for open boundaries, the simulation domain is terminated by an absorbing layer of thickness t_{AB} [37]. As confining potential for the straight waveguides, a hyperbolic secant potential is employed

$$V(x,y) = -\frac{V_0}{\cosh(\beta x)}, \tag{20}$$

with $\beta = \frac{2\,\text{arccosh}(2)}{W}$, W the full width at half maximum, and V_0 the potential depth. In practice, this potential profile can be realized approximately by means of a wire suspended above the graphene plane [7]. In addition to being relevant for top-gated structures, this potential also has the advantage of supporting analytical solutions for the eigenmodes [7],

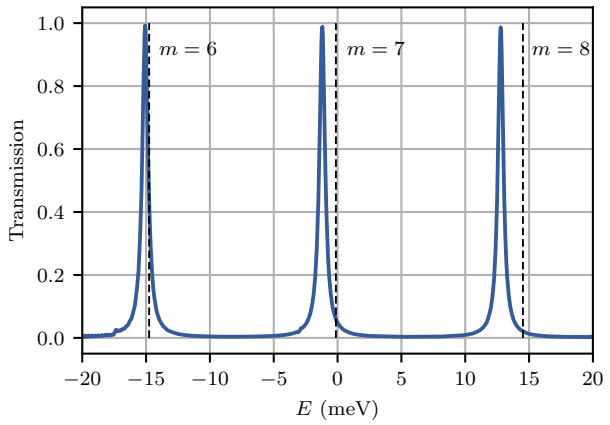

Fig. 3. Transmission as a function of energy E from the lower right waveguide segment (source) to the lower left segment (observer).

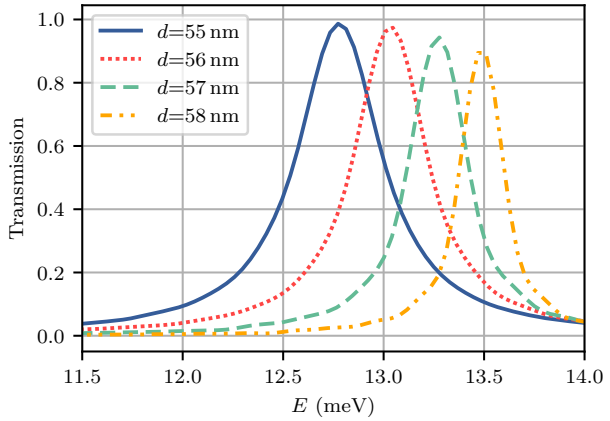

Fig. 4. Transmission as a function of energy E from the lower right waveguide segment (source) to the lower left segment (observer) for different values of the distance d between the center of the ring and the waveguide.

allowing us to validate the eigenmode solver. As value for W, 8 nm was employed, which — according to [24] — is a realistic value. Note that this characteristic length of the potential is much larger than 0.142 nm, the length of the bonds in graphene, allowing us to neglect intervalley scattering [9]. The parameter V_0 equals 0.25 eV, leading to a waveguide supporting only a single bound mode for the energy range of interest. The potential of the dot is given by

$$V(x,y) = \begin{cases} -V_1, & \text{if } r < R, \\ -\frac{V_1}{\cosh(\beta(r-R))}, & \text{otherwise,} \end{cases} \tag{21}$$

where V_1 equals 0.15 eV. For the simulations presented in this section, the following values of the other parameters are used: $d = 55$ nm, $L = 200$ nm, $R = 45$ nm, $t_{\text{AB}} = 80$ nm, $\sigma_t = 80$ fs, and $t_0 = 480$ fs and the simulation domain is discretized using 15 cells per wavelength λ ($= 2\pi/k_y$, with k_y the eigenvalue of the eigenmode injected into the waveguide at the source). The parameters of the dot were chosen in such a way that only the first-order eigenmode is excited. The eigenvalue problem associated with the dot is discussed in the Appendix.

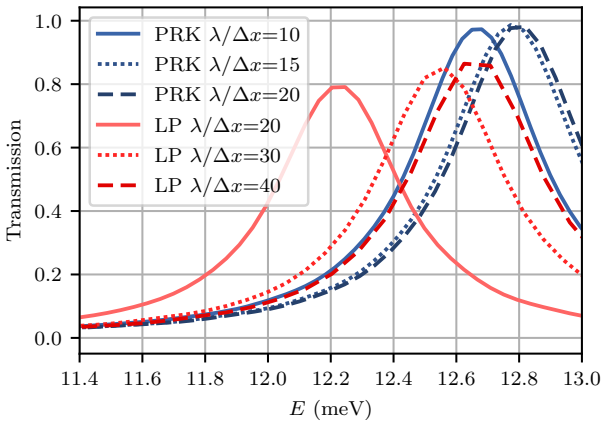

Fig. 5. Comparison between the transmission calculated by means of the presented PRK method and the leapfrog method of [26] for a varying number of grid cells per wavelength ($\lambda/\Delta x$).

A first simulation result is presented in Fig. 3. The transmission as a function of energy from the lower right waveguide segment (source) to the lower left segment (observer), represented by the blue, solid curve, exhibits some clear resonance peaks. For specific values of the energy, the incident mode is fully transmitted to the observer. In addition, the energies of the eigenmodes of the dot have been marked by the dashed lines. As pointed out in the Appendix, these can be calculated directly by means of the same eigenmode solver (see Section III), albeit with a transformed electrostatic potential. It is noted that the resonance peaks are slightly offset from the ideal theoretical prediction. This is to be expected because the waveguides consist of a smooth potential of which its tails extend well into the dot, thus affecting the confining potential of the dot. To check this hypothesis, the distance d between the center of the dot and the waveguide is varied in Fig. 4. By increasing this distance, the resonance peak indeed shifts towards higher values of the energy, i.e., towards the expected position of the resonance peak, thereby confirming our hypothesis. In addition, it is also noted that when d is increased, and thus when the coupling is reduced, that the width of the resonance peaks decreases, which is in agreement with the Heisenberg uncertainty principle. Remark that in the same way, the potential depth V_0 can be varied to change the position and width of the resonance peaks.

In Fig. 5 the novel PRK technique is compared to another method, the second-order leapfrog technique from [26], for a varying number of grid cells per wavelength. It is observed that the results of the PRK technique converge faster owing to the higher-order accuracy. Only for a considerably larger amount of grid cells per wavelength (40 instead of 10) the leapfrog method can determine the resonance frequency with an accuracy comparable to that of the PRK method. However, the numerical simulations, performed on a Dell laptop with Intel Core i7 Processor (6×2.70 GHz) and 16 GB RAM, took 1532 s for the leapfrog technique and 365 s for the novel PRK scheme, thus the PRK scheme is more efficient.

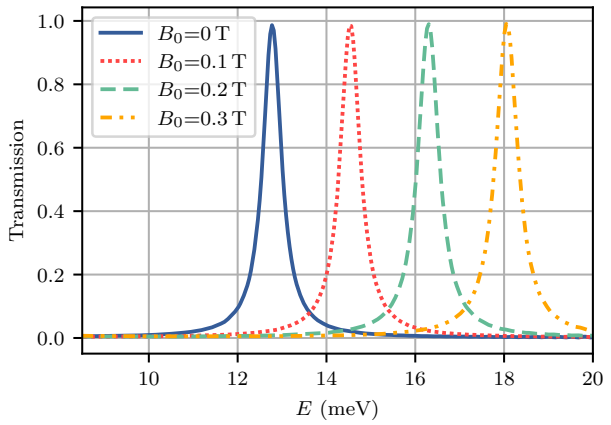

Fig. 6. Transmission as a function of energy E from the lower right waveguide segment (source) to the lower left segment (observer) for different values of B_0, the amplitude of a constant magnetic field perpendicular to the graphene layer.

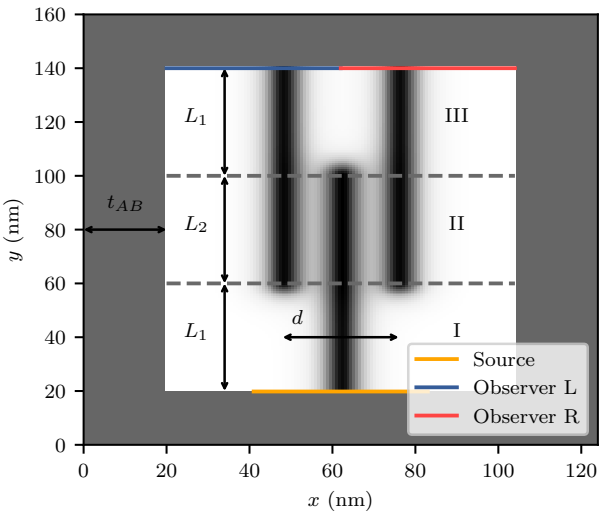

Fig. 7. Simulation setup of splitter consisting of three straight waveguide segments.

In addition, the leapfrog systematically underestimates the height of the transmission resonance. Therefore, the PRK method is the preferred technique for the simulations of these electrostatically induced waveguide structures in graphene.

To demonstrate that the resonance peaks can also be tuned by means of a vector potential, an additional constant magnetic field perpendicular to the graphene layer $\boldsymbol{B} = B_0 \boldsymbol{u}_z$ is introduced. As corresponding polar components of the vector potential, we take $A_r = 0$ and $A_\theta = \frac{B_0 r}{2}$. This means that the eigenvalue problem for the dot now changes from (A.5) into

$$(E - V)\begin{pmatrix}\tilde{u}\\ \tilde{v}\end{pmatrix} = v_F\left[-i\hbar\sigma_x\frac{\partial}{\partial r} + \hbar\sigma_y\frac{(m+1/2)\hbar - qB_0 r^2/2}{r}\right]\begin{pmatrix}\tilde{u}\\ \tilde{v}\end{pmatrix}, \tag{22}$$

where m should be an integer value for $\left(\begin{smallmatrix}\tilde{u}\\ \tilde{v}\end{smallmatrix}\right)$ to be an eigenmode as explained in the Appendix. Equation (22) indicates that when a constant magnetic field is introduced, m will be shifted. Consequently, to match the requirement that m is integer, the resonance energy needs to shift as well. To check this behavior an additional set of simulations is performed with the angular component of the vector potential A_θ equal to $\frac{B_0 r}{2}$. The results are displayed in Fig. 6 and agree with the expectations. The resonance peaks are shifted and the size of the shift is determined by the magnitude of the magnetic field. These results indicate that the magnetic field introduces an additional degree of freedom to tailor the properties of the device.

B. Splitter

The next example that is considered in this paper is the splitter. In [38] a Y-shaped splitter was proposed and investigated numerically. The presented splitter contains several bends, while only straight potential wells have been realized yet in graphene [24]. Therefore, we consider a different structure

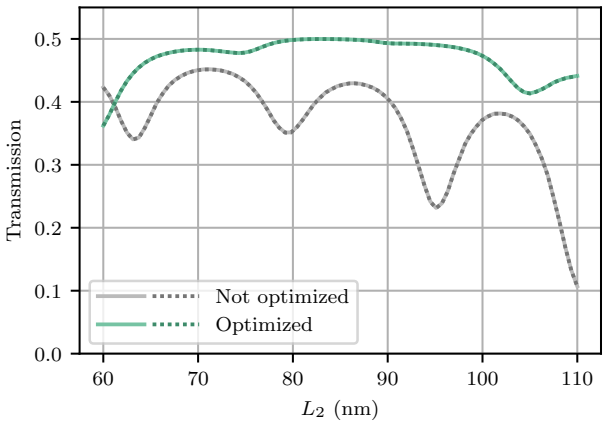

Fig. 8. Transmission through the splitter as a function of the length L_2 of region II for the standard and optimized situation. The solid and dotted lines represent the left observer and right observer of this device, respectively.

instead, consisting only of straight waveguide segments. The setup is depicted in Fig. 7. A mode propagating along the positive y-direction is injected at the source in the bottom waveguide segment (region I). In region II of length L_2 it couples into the two other waveguides. By carefully tuning L_2 the performance of the splitter is optimized such that the current is transmitted towards the two observers, which are positioned in region III, in equal proportions of 0.5.

For the simulations the hyperbolic secant potential is again employed with parameters $W = 8\,\text{nm}$ and $V_0 = 0.25\,\text{eV}$. For the other parameters the following values are used: $d = 28\,\text{nm}$, $L_1 = 25\,\text{nm}$, $E = 0.03\,\text{eV}$, $t_{\text{AB}} = 80\,\text{nm}$, $\sigma_t = 80\,\text{fs}$, and $t_0 = 480\,\text{fs}$. To discretize the simulation domain 15 cells per wavelength are chosen. For these values, the transmission to the two observers as a function of L_2 is represented by the grey solid and dotted line in Fig. 8. For every value of L_2, the transmission is significantly below 0.5, indicating that

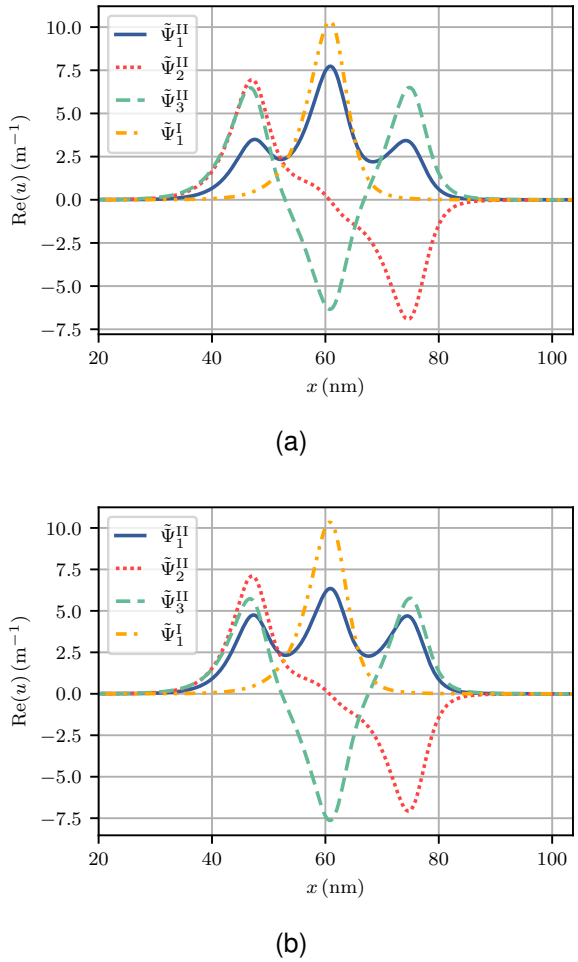

Fig. 9. Real part of the three lowest-order eigenmodes of region II and the lowest-order eigenmode of region I for the standard (a) and optimized (b) situation.

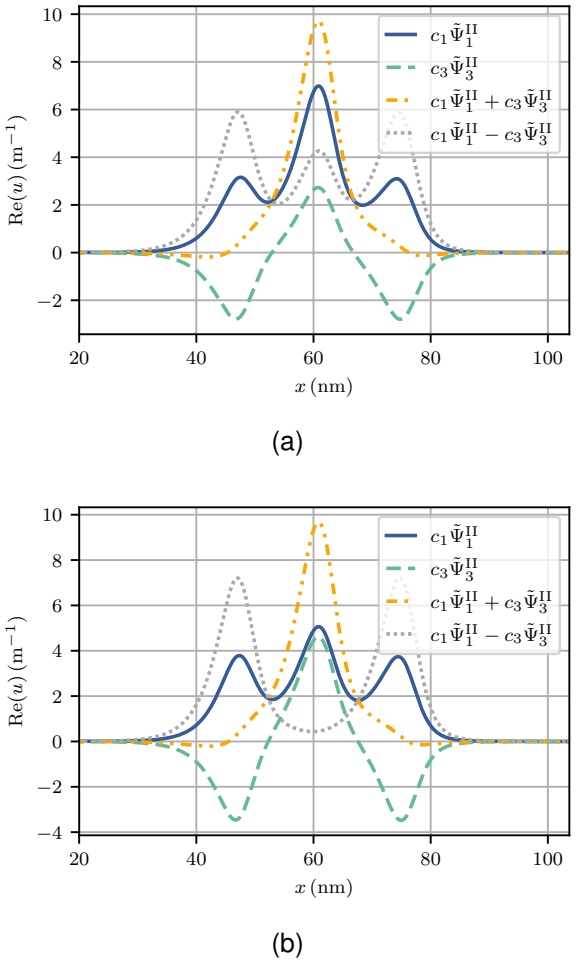

Fig. 10. Real part of the first component u of $c_1\tilde{\Psi}_1^{\mathrm{II}}$, $c_3\tilde{\Psi}_3^{\mathrm{II}}$, $c_1\tilde{\Psi}_1^{\mathrm{II}} + c_3\tilde{\Psi}_3^{\mathrm{II}}$, and $c_1\tilde{\Psi}_1^{\mathrm{II}} - c_3\tilde{\Psi}_3^{\mathrm{II}}$ for the standard (a) and optimized (b) situation.

the coupling to the two outgoing waveguides is suboptimal. To explain these results, the normalized, three lowest-order eigenmodes of region II and lowest-order eigenmode of region I are plotted as a function of x in Fig. 9a. At the source the first-order mode $\tilde{\mathbf{\Psi}}_1^{\mathrm{I}}$ is injected into the waveguide. From mode matching theory we know that this incoming mode will excite a linear combination of eigenmodes in region II. Since the incoming mode is symmetric, the expansion coefficient related to the anti-symmetric second-order mode $\tilde{\mathbf{\Psi}}_2^{\mathrm{II}}$ is zero. Consequently, at the boundary between region I and II, the linear combination of excited modes in region II can be approximated, up to a phase factor, as $c_1\tilde{\mathbf{\Psi}}_1^{\mathrm{II}} + c_3\tilde{\mathbf{\Psi}}_3^{\mathrm{II}}$, with $c_1 = \langle\tilde{\mathbf{\Psi}}_1^{\mathrm{II}}, \tilde{\mathbf{\Psi}}_1^{\mathrm{I}}\rangle / \langle\tilde{\mathbf{\Psi}}_1^{\mathrm{II}}, \tilde{\mathbf{\Psi}}_1^{\mathrm{II}}\rangle$ and likewise for c_3. The eigenvalues related to the eigenmodes $\tilde{\mathbf{\Psi}}_1^{\mathrm{II}}$ and $\tilde{\mathbf{\Psi}}_3^{\mathrm{II}}$ are $k_{y,1}^{\mathrm{II}} = 0.318\,\mathrm{nm}^{-1}$ and $k_{y,3}^{\mathrm{II}} = 0.278\,\mathrm{nm}^{-1}$, respectively. Because the incoming mode is solely confined to the central waveguide, the off-center peaks of $c_1\tilde{\mathbf{\Psi}}_1^{\mathrm{II}}$ and $c_3\tilde{\mathbf{\Psi}}_3^{\mathrm{II}}$ (located at $x \approx 46\,\mathrm{nm}$ and $x \approx 74\,\mathrm{nm}$) cancel each other out, which is illustrated by the orange line of Fig. 10a. At the interface between region II and region III, the opposite situation, i.e., the main peaks cancel while the off-center peaks add up, is desired. When choosing L_2 equal to $\pi/(k_{y,1} - k_{y,3}) \approx 78.5\,\mathrm{nm}$, the expansion coefficients will have switched sign with respect to each other and the central peaks will now cancel, however, only partially. This situation is represented by the grey dotted line of Fig. 10a, where it is seen that the difference $c_1\tilde{\Psi}_1^{\mathrm{II}} - c_3\tilde{\Psi}_3^{\mathrm{II}}$ still exhibits a relatively large peak at $x \approx 60\,\mathrm{nm}$, explaining the suboptimal transmission of Fig. 8.

One of the main strengths, though, of electrostatically induced waveguide devices is their tunability. By simply changing the electrostatic potential, the properties of the waveguide can be modified. Therefore, we change the value of V_0 for the left and right electrostatic potential from $0.25\,\mathrm{eV}$ to $0.2625\,\mathrm{eV}$. The resulting eigenmodes $\tilde{\mathbf{\Psi}}_1^{\mathrm{II}}$, $\tilde{\mathbf{\Psi}}_2^{\mathrm{II}}$, and $\tilde{\mathbf{\Psi}}_3^{\mathrm{II}}$, with related eigenvalues $k_{y,1}^{\mathrm{II}} = 0.325\,\mathrm{nm}^{-1}$, $k_{y,2}^{\mathrm{II}} = 0.312\,\mathrm{nm}^{-1}$, and $k_{y,3}^{\mathrm{II}} = 0.291\,\mathrm{nm}^{-1}$, respectively, are plotted in Fig. 9b. The optimal length of L_2 is now given by $92.4\,\mathrm{nm}$ for the theoretical case of sharp potential steps to terminate the waveguides at the end. For this optimized situation, the difference $c_1\tilde{\Psi}_1^{\mathrm{II}} - c_3\tilde{\Psi}_3^{\mathrm{II}}$ does not exhibit a peak anymore at $x \approx 60\,\mathrm{nm}$ (Fig. 10b). Consequently, as demonstrated in Fig. 8, the transmission of this optimized setup now indeed reaches the maximum of 0.5, and thus the device of Fig. 7 functions as an ideal splitter. Note that the maximum of 0.5 is positioned at a value of L_2 slightly below the theoretical one. As the three potentials are not terminated abruptly, but rather smoothly, the

effective coupling length is slightly longer than L_2.

V. Conclusion

In this paper, we have presented a novel technique based on higher-order conservative partitioned Runge-Kutta time stepping, adapted to the analysis of electronic waveguide devices in graphene. It was demonstrated that the excellent long-term properties of the time stepping scheme are retained in the presence of a vector potential. Additionally, a theoretical study of the eigenmode problem in the waveguide was presented, which is necessary to define and physically interpret the transmission properties. Subsequently, this technique was applied to the study of two examples: a dot resonator and a splitter. The dot resonator exhibited frequency selective behavior that proved to be tunable by both the scalar and vector potential. Additionally, the results were considerably more accurate than those obtained with second-order leapfrog method, illustrating the higher-order accuracy of the constructed technique. A 50/50 splitter topology in graphene was discussed containing no bends. By carefully modifying the properties of the waveguides, which is possible thanks to their highly tunable nature, the desired output characteristic was obtained.

Acknowledgment

The authors would like to thank Research Foundation - Flanders (FWO) for supporting this research (1107321N).

Appendix
Eigenmodes of a dot

To determine the eigenmodes of the dot, the Dirac equation (1) is first transformed from Cartesian coordinates (x, y) to polar coordinates (r, θ). Hence, $\boldsymbol{\nabla}$ equals $\frac{\partial}{\partial r}\boldsymbol{u}_r + \frac{1}{r}\frac{\partial}{\partial \theta}\boldsymbol{u}_\theta$, while $\boldsymbol{\sigma} = \sigma_r \boldsymbol{u}_r + \sigma_\theta \boldsymbol{u}_\theta$ and $\boldsymbol{a} = a_r \boldsymbol{u}_r + a_\theta \boldsymbol{u}_\theta$. Given that

$$\begin{pmatrix} \boldsymbol{u}_r \\ \boldsymbol{u}_\theta \end{pmatrix} = \begin{pmatrix} \cos\theta & \sin\theta \\ -\sin\theta & \cos\theta \end{pmatrix} \begin{pmatrix} \boldsymbol{u}_x \\ \boldsymbol{u}_y \end{pmatrix}, \tag{A.1}$$

it is readily shown that

$$\sigma_r = \begin{pmatrix} 0 & e^{-i\theta} \\ e^{i\theta} & 0 \end{pmatrix} \quad \text{and} \quad \sigma_\theta = \begin{pmatrix} 0 & -ie^{-i\theta} \\ ie^{i\theta} & 0 \end{pmatrix}. \tag{A.2}$$

Substituting these expressions into (1), yields the Dirac equation in polar coordinates:

$$\begin{aligned} i\hbar\frac{\partial}{\partial t}u &= v_F\, e^{-i\theta}\left[-i\hbar\frac{\partial}{\partial r} - \frac{\hbar}{r}\frac{\partial}{\partial\theta} - qa_r + iqa_\theta\right] v + V\, u \\ i\hbar\frac{\partial}{\partial t}v &= v_F\, e^{i\theta}\left[-i\hbar\frac{\partial}{\partial r} + \frac{\hbar}{r}\frac{\partial}{\partial\theta} - qa_r - iqa_\theta\right] u + V\, v. \end{aligned} \tag{A.3}$$

As the electrostatic potential is rotationally symmetric, it only depends on the variable r. Additionally, assume that the vector potential is zero. Then, consider the following ansatz for the wave function [18]

$$\begin{pmatrix} u(r,\theta,t) \\ v(r,\theta,t) \end{pmatrix} = \frac{e^{iEt/\hbar}}{\sqrt{r}} \begin{pmatrix} e^{i(m-1)\theta}\,\tilde{u}(r) \\ e^{im\theta}\,\tilde{v}(r) \end{pmatrix}. \tag{A.4}$$

Consequently, by employing (A.4), (A.3) is rewritten into

$$\begin{aligned} (E - V)\begin{pmatrix} \tilde{u}(r) \\ \tilde{v}(r) \end{pmatrix} = \\ v_F\left[-i\hbar\,\sigma_x\frac{\partial}{\partial r} + \hbar\,\sigma_y\frac{m+1/2}{r}\right]\begin{pmatrix} \tilde{u}(r) \\ \tilde{v}(r) \end{pmatrix}, \end{aligned} \tag{A.5}$$

which constitutes an eigenvalue problem, with as eigenvalue m. Remark that $u\,(r, \theta, t)$ equals $u\,(r, \theta + 2\pi, t)$, which means that m should be an integer number and thus, that only for specific values of the energy E an eigenmode can be found. Equation (A.5) can be discretized directly and solved via numerical techniques. Here, however, we adopt a slightly different approach. We additionally apply the following conformal transformation [39]

$$r = R_c\, e^{x'/R_c}, \tag{A.6}$$

with R_c a constant, to (A.5), yielding

$$\begin{aligned} (E - V)\, e^{x'/R_c}\begin{pmatrix} \tilde{u}(x') \\ \tilde{v}(x') \end{pmatrix} = \\ v_F\left[-i\hbar\,\sigma_x\frac{\partial}{\partial x'} + \hbar\,\sigma_y\frac{m+1/2}{R_c}\right]\begin{pmatrix} \tilde{u}(x') \\ \tilde{v}(x') \end{pmatrix}, \end{aligned} \tag{A.7}$$

which can be rearranged into the exact same form as (4) allowing us to reuse the same numerical method as for the straight waveguides.

References

[1] W. Steinhögl, G. Schindler, G. Steinlesberger, M. Traving, and M. Engelhardt, "Comprehensive study of the resistivity of copper wires with lateral dimensions of 100 nm and smaller," *J. Appl. Phys.*, vol. 97, pp. 1–7, Jan. 2005.

[2] D. Josell, S. H. Brongersma, and Z. Tokei, "Size-dependent resistivity in nanoscale interconnects," *Annu. Rev. Mater. Res.*, vol. 39, pp. 231–254, Aug. 2009.

[3] W. Cao, J. Jiang, X. Xie, A. Pal, J. H. Chu, J. Kang, and K. Banerjee, "2-D Layered Materials for Next-Generation Electronics: Opportunities and Challenges," *IEEE Trans. Electron Devices*, vol. 65, pp. 4109–4121, Oct. 2018.

[4] W. S. Zhao, K. Fu, D. W. Wang, M. Li, G. Wang, and W. Y. Yin, "Mini-review: Modeling and performance analysis of nanocarbon interconnects," *Appl. Sci.*, vol. 9, pp. 3–21, May 2019.

[5] H. Li, C. Xu, N. Srivastava, and K. Banerjee, "Carbon Nanomaterials for Next-Generation Interconnects and Passives: Physics, Status, and Prospects," *IEEE Trans. Electron Devices*, vol. 56, pp. 1799–1821, Sep. 2009.

[6] V. R. Kumbhare, R. Kumar, M. K. Majumder, S. Kumar, P. P. Paltani, B. K. Kaushik, and R. Sharma, "High-Speed Interconnects: History, Evolution, and the Road Ahead," *IEEE Microw. Mag.*, vol. 23, pp. 66–82, Aug. 2022.

[7] R. R. Hartmann, N. J. Robinson, and M. E. Portnoi, "Smooth electron waveguides in graphene," *Phys. Rev. B*, vol. 81, Jun. 2010.

[8] P. Rickhaus, M. H. Liu, P. Makk, R. Maurand, S. Hess, S. Zihlmann, M. Weiss, K. Richter, and C. Schönenberger, "Guiding of Electrons in a Few-Mode Ballistic Graphene Channel," *Nano Lett.*, vol. 15, pp. 5819–5825, Sep. 2015.

[9] P. E. Allain and J. N. Fuchs, "Klein tunneling in graphene: Optics with massless electrons," *Eur. Phys. J. B*, vol. 83, pp. 301–317, Oct. 2011.

[10] S. Chen, Z. Han, M. M. Elahi, K. M. M. Habib, L. Wang, B. Wen, Y. Gao, T. Taniguchi, K. Watanabe, J. Hone, A. W. Ghosh, and C. R. Dean, "Electron optics with p-n junctions in ballistic graphene," *Science*, vol. 353, pp. 1522–1525, Sep. 2016.

[11] V. Cheianov, V. Fal'ko, and B. L. Altshuler, "The Focusing of Electron Flow and a Veselago Lens in Graphene p-n Junctions," *Science*, vol. 315, pp. 1252–1255, May 2007.

[12] P. Rickhaus, R. Maurand, M. H. Liu, M. Weiss, K. Richter, and C. Schönenberger, "Ballistic interferences in suspended graphene," *Nat. Commun.*, vol. 4, pp. 1–6, Aug. 2013.

[13] Q. Wilmart, S. Berrada, D. Torrin, V. H. Nguyen, G. Fève, J. M. Berroir, P. Dollfus, and B. Plaçais, "A Klein-tunneling transistor with ballistic graphene," *2D Mater.*, vol. 1, Apr. 2014.

[14] R. N. Sajjad and A. W. Ghosh, "Manipulating chiral transmission by gate geometry: Switching in graphene with transmission gaps," *ACS Nano*, vol. 7, pp. 9808–9813, Nov. 2013.

[15] P. Wan, Y. Ren, Q. Wang, D. Huang, L. Zhou, H. Guo, and J. Du, "Dirac fermion metagratings in graphene," *NPJ 2D Mater. Appl.*, vol. 5, pp. 1–7, Dec. 2021.

[16] R. Zhao, P. Wan, L. Zhou, D. Huang, H. Guo, H. Xia, and J. Du, "Electron metasurfaces in graphene," *Phys. Rev. B*, vol. 107, pp. 1–9, Apr. 2023.

[17] J. M. Caridad, S. Connaughton, C. Ott, H. B. Weber, and V. Krstić, "An electrical analogy to Mie scattering," *Nat. Commun.*, vol. 7, pp. 1–6, Sep 2016.

[18] Y. Zhao, J. Wyrick, F. D. Natterer, J. F. Rodriguez-Nieva, C. Lewandowski, K. Watanabe, T. Taniguchi, L. S. Levitov, N. B. Zhitenev, and J. A. Stroscio, "Creating and probing electron whispering-gallery modes in graphene," *Science*, vol. 348, pp. 672–675, May 2015.

[19] B. Brun, V. H. Nguyen, N. Moreau, S. Somanchi, K. Watanabe, T. Taniguchi, J. C. Charlier, C. Stampfer, and B. Hackens, "Graphene Whisperitronics: Transducing Whispering Gallery Modes into Electronic Transport," *Nano Lett.*, vol. 22, pp. 128–134, Jan. 2022.

[20] Z. B. Zhang, R. Wang, B. Wang, and D. Y. Xing, "Quantum Goos-Hänchen switch in graphene junctions," *New J. Phys.*, vol. 25, pp. 1–13, Dec. 2023.

[21] M. Yankowitz, J. Xue, and B. J. Leroy, "Graphene on hexagonal boron nitride," *J. Phys. Condens. Matter*, vol. 26, pp. 1–21, Jul. 2014.

[22] J. Xue, J. Sanchez-Yamagishi, D. Bulmash, P. Jacquod, A. Deshpande, K. Watanabe, T. Taniguchi, P. Jarillo-Herrero, and B. J. Leroy, "Scanning tunnelling microscopy and spectroscopy of ultra-flat graphene on hexagonal boron nitride," *Nat. Mater.*, vol. 10, pp. 282–285, Apr. 2011.

[23] C. R. Dean, A. F. Young, I. Meric, C. Lee, L. Wang, S. Sorgenfrei, K. Watanabe, T. Taniguchi, P. Kim, K. L. Shepard, and J. Hone, "Boron nitride substrates for high quality graphene electronics," *Nat. Nanotechnol.*, vol. 5, pp. 722–726, Oct. 2010.

[24] A. Cheng, T. Taniguchi, K. Watanabe, P. Kim, and J. D. Pillet, "Guiding Dirac Fermions in Graphene with a Carbon Nanotube," *Phys. Rev. Lett.*, vol. 123, pp. 1–6, Nov. 2019.

[25] E. Vanderstraeten and D. Vande Ginste, "Analysis of Electrostatically Induced Interconnect Structures in Single-Layer Graphene via a Conservative First-Principles Modeling Technique," in *Proc. IEEE 32st Conf. Elect. Perform. Electron. Packag. Syst.*, Milpitas, USA, Oct. 2023, pp. 1–3.

[26] R. Hammer, W. Pötz, and A. Arnold, "Single-cone real-space finite difference scheme for the time-dependent Dirac equation," *J. Comput. Phys.*, vol. 265, pp. 50–70, May 2014.

[27] E. Vanderstraeten and D. Vande Ginste, "A conservative fourth-order real space method for the (2+1)D Dirac equation," *J. Comput. Appl. Math.*, vol. 428, pp. 1–19, Aug. 2023.

[28] F. M. Zhang, Y. He, and X. Chen, "Guided modes in graphene waveguides," *Appl. Phys. Lett.*, vol. 94, pp. 1–3, May 2009.

[29] P. Peng, P. Zhang, J. K. Liu, Z. Z. Cao, and G. Q. Li, "Oscillating guided modes in graphene-based asymmetric waveguides," *Commun. Theor. Phys.*, vol. 58, pp. 765–771, Nov. 2012.

[30] Y. He, M. Ding, Y. Yang, and H. Zhang, "Guided modes in a graphene barrier waveguide," *Superlattices Microstruct.*, vol. 85, pp. 761–767, Sep. 2015.

[31] R. R. Hartmann and M. E. Portnoi, "Quasi-exact solution to the Dirac equation for the hyperbolic-secant potential," *Phys. Rev. A*, vol. 89, pp. 1–7, Jan. 2014.

[32] ——, "Two-dimensional Dirac particles in a Pöschl-Teller waveguide," *Sci. Rep.*, vol. 7, pp. 1–10, Sep. 2017.

[33] J. G. Van Bladel, *Electromagnetic Fields*, 2nd ed. Wiley-IEEE Press, 2007.

[34] J. M. Sanz-Serna and M. P. Calvo, *Numerical Hamiltonian Problems*, 1st ed. Chapman & Hall, London, U.K, 1994.

[35] R. I. McLachlan, "On the Numerical Integration of Ordinary Differential Equations by Symmetric Composition Methods," *SIAM J. Sci. Comput.*, vol. 16, pp. 151–168, Jan. 1995.

[36] W. Bogaerts, P. de Heyn, T. van Vaerenbergh, K. de Vos, S. K. Selvaraja, T. Claes, P. Dumon, P. Bienstman, D. van Thourhout, and R. Baets, "Silicon microring resonators," *Laser and Photonics Reviews*, vol. 6, pp. 47–73, Jan. 2012.

[37] O. Pinaud, "Absorbing layers for the Dirac equation," *J. Comput. Phys.*, vol. 289, pp. 169–180, May 2015.

[38] V. Mosallanejad, K. L. Chiu, and G. ping Guo, "Coherent transport in Y-junction graphene waveguide," *J. Phys. Condens. Matter*, vol. 30, pp. 1–8, Oct. 2018.

[39] M. Heiblum and J. H. Harris, "Analysis of Curved Optical Waveguides by Conformal Transformation," *IEEE J. Quantum Electron.*, vol. 11, pp. 75–83, Feb. 1975.